

Realizing Wide-Gamut Human-Centric Display Lighting with $\text{K}_3\text{AlP}_3\text{O}_9\text{N:Eu}^{2+}$

Shruti Hariyani, Xinxin Xing, Mahdi Amachraa, Jiming Bao, Shyue Ping Ong, and Jakoah Brgoch*


Computers, televisions, and smartphones are revolutionized by the invention of InGaN blue light-emitting diode (LED) backlighting. Yet, continual exposure to the intense blue LED emission from these modern displays can cause insomnia and mood disorders. Developing “human-centric” backlighting that uses a violet-emitting LED chip and a trichromatic phosphor mixture to generate color images is one approach that addresses this problem. The challenge is finding a blue-emitting phosphor that possesses a sufficiently small Stokes’ shift to efficiently down-convert violet LED light and produce a narrow blue emission. This work reports a new oxynitride phosphor that meets this demand. $\text{K}_3\text{AlP}_3\text{O}_9\text{N:Eu}^{2+}$ exhibits an unexpectedly narrow (45 nm, 2206 cm^{-1}), thermally robust, and efficient blue photoluminescence upon violet excitation. Computational modeling and temperature-dependent optical property measurements reveal that the narrow emission arises from a rare combination of preferential excitation and site-selective quenching. The resulting chromaticity coordinates of $\text{K}_3\text{AlP}_3\text{O}_9\text{N:Eu}^{2+}$ lie closer to the vertex of the Rec. 2020 than a blue LED chip and provides access to $\approx 10\%$ more colors than a commercial tablet when combined with commercial red- and green-emitting phosphors. Alongside the wide gamut, tuning the emission from the violet LED and phosphor blend can reduce blue light emissions to produce next-generation, human-centric displays.

S. Hariyani, J. Brgoch
Department of Chemistry
University of Houston
Houston, TX 77204, USA
E-mail: jbrgoch@uh.edu

S. Hariyani, J. Bao, J. Brgoch
Texas Center for Superconductivity
University of Houston
Houston, TX 77204, USA

X. Xing, J. Bao
Department of Electrical and Computer Engineering
University of Houston
Houston, TX 77204, USA

M. Amachraa, S. P. Ong
Department of NanoEngineering
University of California San Diego
La Jolla, CA 92093, USA

 The ORCID identification number(s) for the author(s) of this article can be found under <https://doi.org/10.1002/adom.202202689>.

DOI: 10.1002/adom.202202689

1. Introduction

Modern light-emitting diode (LED)-based displays, including televisions, monitors, tablets, and smartphones, operate by partially down-converting a blue-emitting (InGa)N LED chip using green- and red-emitting rare-earth or transition-metal substituted inorganic phosphors or quantum dots.^[1] The red, green, and blue (RGB) colors produced by the three emission peaks make up the (white-emitting) backlight, which is then passed through a series of filters creating colored images.^[2] One of the requirements, among many, vital for optimizing a display’s properties is that the LED and phosphors must all possess ultra-narrow emission bands. This allows the entirety of the emission band to be transmitted through the color filters so that the display can achieve saturated chromaticity coordinates and cover a wide color gamut, or the range of colors a display can produce.^[2] The current industry standard color gamut is the ITU-R recommendation BT. 2020 standard (Rec. 2020), which is far larger than the traditional

National Television System Committee (NTSC) color gamut.^[3] Today, the saturated blue corner of the Rec. 2020 gamut is nearly satisfied by the LED emission, whereas the red corner is covered by phosphors such as $\text{K}_2\text{SiF}_6\text{:Mn}^{4+}$, $\text{Sr}[\text{LiAl}_3\text{N}_4]\text{:Eu}^{2+}$, $\text{CaAlSiN}_3\text{:Eu}^{2+}$ or InP-based quantum dots.^[4] The green color is usually generated by $\beta\text{-SiAlON:Eu}^{2+}$; however, this material generates far from optimal Rec. 2020 coverage leading to significant effort on new phosphor discovery.^[5]

Regardless, LED lighting is not problem-free. It has been recently shown that continual blue-light exposure can disrupt our natural circadian rhythm by suppressing melatonin production through interactions with the intrinsic photorectal ganglion cells.^[6] Links have also been made between blue light and insomnia, mood disorders, and macular degeneration.^[7] The blue-emitting LED component of today’s TV and phone screens has thus been surreptitiously impacting our health. Indeed, the white backlight from an Apple iPad contains an intense blue LED emission that not only overlaps with the maximum of a wavelength-dependent melatonin suppression curve (Figure 1a, in gray), but on high-brightness mode, this blue light can also leak through and create blue-tinted images.^[8] This is becoming

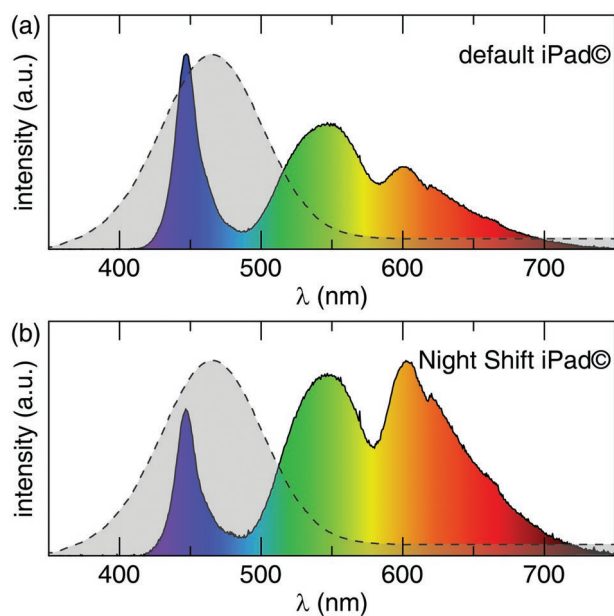


Figure 1. a) The white light spectrum from an 8th generation Apple iPad using the default color temperature setting is dominated by the blue LED emission which overlaps with a wavelength-dependent melatonin suppression curve (dashed, grey). b) Turning on night shift with the default color temperature setting on maximum brightness produces warmer-toned images by increasing the ratio of red light emitted, but the intense blue LED emission prevails.

a serious problem considering an estimated 90% of Americans look at some type of screen before bed.^[9] As a result, electronic modifications, such as Night Shift by Apple Inc. have been introduced to combat this “blue light hazard.” The software adjusts the screen’s blue:red light ratio producing warmer-toned images. However, analyzing the backlight emission spectrum of an iPad on high brightness mode with Night Shift[®] on still shows a prominent blue LED peak (Figure 1b). Studies have shown that this resulting blue LED emission causes $\approx 10\%$ melatonin suppression after only 1 h of exposure, likely due to persistent blue light leakage.^[8] It is clear that alternative methods to reduce blue light exposure from LED-driven displays must be considered.

“Human-centric” lighting aims to minimize the negative impacts of continual blue light exposure from LED-based technologies. One proposed method involves shifting these devices to a violet LED ($\lambda_{\text{em}} \approx 400$ nm) pump coupled with a trichromatic phosphor blend (red-, green-, and blue-emitting). It is important to note that red-, green-, and blue-emitting components are always required to create a white light spectrum. However, moving from a blue LED light source to a blue-emitting phosphor enables a reduction in the amount of excess blue-light that can be leaked from the package thereby minimizing “blue-light hazard.” The result is still an intense, energy-efficient, broad-spectrum white light.^[10] This approach has already been successfully applied to create a prototype human-centric warm white LED light bulb with better color rendering than a commercial bulb with a minimal blue light component.^[11] Curiously, a similar approach for LED-based display backlighting has not yet been discussed, but it undoubtedly needs to be addressed considering that American children spend an estimated 7.5 h daily looking at screens.^[12]

One factor limiting the widespread conversion to human-centric displays is the lack of phosphors that possess the small Stokes’ shift necessary to achieve blue emission upon violet excitation. It is also essential for a display phosphor to have a narrow emission full width at half maximum (fwhm < 50 nm), enabling the chromaticity coordinates to cover the blue vertex of the Rec. 2020. The most popular blue-emitting phosphor and arguably the most viable blue component for human-centric display lighting is $\text{BaMgAl}_{10}\text{O}_{17}:\text{Eu}^{2+}$ (BAM:Eu²⁺).^[13] This industry-standard phosphor has a 90% photoluminescent quantum yield (PLQY) and a moderately narrow fwhm of 51 nm (2532 cm^{-1}) under 400 nm excitation. The main drawback of $\text{BaMgAl}_{10}\text{O}_{17}:\text{Eu}^{2+}$ is its poor chemical stability.^[14] The emission spectrum of commercially purchased $\text{BaMgAl}_{10}\text{O}_{17}:\text{Eu}^{2+}$ red-shifts and broadens by $\approx 10\%$ upon long term water exposure, causing the chromaticity coordinates to move away from the deep-blue corner of the Rec. 2020.^[11] $\text{Na}_2\text{MgPO}_4\text{F}:\text{Eu}^{2+}$ is far more chemically stable, but its broad fwhm (79 nm; 3782 cm^{-1}) precludes it from display applications.^[11] A new nitridophosphide phosphor, $\text{SrP}_8\text{N}_{14}:\text{Eu}^{2+}$, was reported to produce an ultra-narrow blue emission ($\lambda_{\text{em}} = 440$ nm) with a fwhm of only 26 nm (1350 nm^{-1}).^[15] This material is promising but it requires air-sensitive reagents and high pressure during synthesis, making mass production challenging. Clearly, further research is necessary to identify an application-ready, blue-emitting phosphor for violet-pumped human-centric display backlighting.

The success of the nitridophosphide phosphor inspired the search of another underexplored class of materials, phosphorous oxynitrides. Unlike pure nitrides, phosphorous oxynitrides can be produced using oxide precursors and nitridating in situ by flowing ammonia over the reactants.^[16] Few compounds are known within this composition space, but a family of oxynitrides following the $\text{M}_3\text{M}^{\text{III}}\text{P}_3\text{O}_9\text{N}$ ($\text{M}^{\text{I}} = \text{Na, K}; \text{M}^{\text{III}} = \text{Al, In, Ga, Ti, V, Cr, Mn, Fe}$) general formula can be prepared through gas reduction nitridation under flowing NH_3 .^[17] Here, we report the synthesis, structural characterization, and optical properties of one of the materials in this system, Eu^{2+} substituted $\text{K}_3\text{AlP}_3\text{O}_9\text{N}$. This novel phosphor produces a blue emission with a 60(4)% quantum yield under violet light excitation ($\lambda_{\text{ex}} = 400$ nm). The emission spectrum has a fwhm of only 45 nm (2206 cm^{-1}) yielding highly saturated chromaticity coordinates similar to a blue LED. The origin of the narrow emission, established by computational modeling and a comprehensive optical spectroscopy study, stems from a combination of preferential excitation and site-selective quenching. Combining this new blue phosphor with industry-standard red- and green-emitting display phosphors and a violet LED pump create the first wide gamut display backlight with minimal blue light exposure.

2. Methodology

2.1. Materials Synthesis and Optical Characterization

The host crystal structure, $\text{K}_3\text{AlP}_3\text{O}_9\text{N}$, was synthesized by combining KH_2PO_4 (Alfa Aesar, 99%) and Al_2O_3 (Sigma-Aldrich, 99.99%) in the appropriate stoichiometric ratios while the phosphor was obtained by reacting a mixture of KPO_3 and

Al_2O_3 and substituting Eu_2O_3 (Alfa Aesar, 99.99%) following $\text{K}_{3-2x}\text{Eu}_x\text{AlP}_3\text{O}_9\text{N}$ ($x = 0.015, 0.03, 0.06, \text{ and } 0.09$). KPO_3 was prepared by dehydrating KH_2PO_4 (Alfa Aesar, 99.0%) at 350°C for 12 h in air.^[18] The mixtures were first hand-ground using an agate mortar and pestle in an ethanol medium followed by high-energy ball milling for 30 min to ensure homogeneity (Spex 8000 M Mixer/Mill). The precursor powders were then pressed into a 6 mm pellet and placed on a bed of sacrificial powder in an alumina crucible (AdValue Technology). Pure phase synthesis of the phosphor and associated host required annealing the precursor mixture at 800°C for 12 h using a heating and cooling rate of 3°C min^{-1} under flowing NH_3 (anhydrous, Matheson HG G10501250 UN1005).^[16] The heating was repeated twice to ensure high crystallinity and complete nitridation. This reaction should be conducted in a well-ventilated area, like a closed fumehood, due to the use of flowing NH_3 . The NH_3 gas is neutralized after passing through bubblers containing heavy mineral oil and water before being vented into the fumehood.

The resulting products were re-ground into a fine powder using an agate mortar and pestle where preliminary phase purity was checked by powder X-ray diffraction using a Cu $K\alpha$ PanAnalytical X'Pert powder diffractometer ($\lambda = 1.54183 \text{ \AA}$). The host crystal structure and anion ordering were then solved through a joint powder refinement of high-energy synchrotron powder X-ray diffraction from 11-BM at the Advanced Photon Source (APS) at Argonne National Laboratory and neutron powder diffraction using the Spallation Neutron Source (SNS-POWGEN) at Oak Ridge National Laboratory.^[19] The data were collected at 100 K using calibrated wavelengths of 0.458944 \AA and 0.8 \AA , respectively. Co-refinements were performed following the methodology of Denault et al.^[20] The simultaneous refinements were conducted by first adjusting the profile shapes, background (shifted Chebyshev function), and adjusting the instrument parameters. Then, keeping these parameters constant, the unit cell parameters were determined by only refining the synchrotron X-ray diffractogram. The atomic positions were refined using both the X-ray and neutron data jointly. Finally, only the neutron data was used to refine the atomic displacement parameters (ADPs). All Rietveld refinements were performed using the EXPGUI interface of GSAS.^[21] The final crystal structure was visualized using VESTA.^[22]

Polycrystalline samples of $\text{K}_3\text{AlP}_3\text{O}_9\text{N:Eu}^{2+}$ were subsequently mixed with an optically transparent resin (United Adhesives, OP 4036) and deposited onto a quartz slide (Chemglass). The photoluminescent excitation and emission spectra were recorded using a PTI fluorescence spectrophotometer with a 75 W xenon arc lamp for excitation. Temperature-dependent emission spectra (80–640 K) were obtained using a Janis cryostat (VFP – 100). Luminescent measurements at 13 K ($\lambda_{\text{ex}} = 351 \text{ nm}$ and $\lambda_{\text{em}} = 405 \text{ nm}$) were conducted in a closed-cycle refrigerator system made by CRYO industries of America, Inc. The sample was measured by adhering the material on the surface of a copper cold finger in a vacuum. The laser power was maintained at 0.1 mW and the luminescence spectrum was collected by using an iHR 320 spectrometer equipped with a thermoelectric-cooled Synapse charge-coupled device. The room temperature photoluminescent quantum yield was determined using a Spectralon coated integrating sphere

(Labsphere, 150 mm diameter) following the methodology of de Mello et al.^[23] A model white backlight was finally constructed by combining the emissions of $\text{K}_3\text{AlP}_3\text{O}_9\text{N:Eu}^{2+}$ and commercially purchased $\beta\text{-SiAlON:Eu}^{2+}$ (Mitsubishi Chemical Corp.) and $\text{CaAlSiN}_3\text{:Eu}^{2+}$ (Mitsubishi Chemical Corp.) under the excitation from a violet LED ($\lambda_{\text{em}} \approx 395 \text{ nm}$) purchased from Thor Labs (LED395L, 6 mW, TO-18).

2.2. Density Functional Theory Calculations

All density functional theory (DFT) calculations on the $\text{K}_3\text{AlP}_3\text{O}_9\text{N}$ host and Eu^{2+} substituted phosphor were carried out using the Vienna ab initio simulation (VASP) package within the projector-augmented wave (PAW) method.^[24] The generalized gradient approximation Perdew–Burke–Ernzerhof (PBE) functional was used for structural relaxation and energy calculations with a plane wave energy cutoff of 520 eV and the Brillouin zones were integrated with a k -point density grid of at least $100/\text{\AA}^{-3}$ (reciprocal lattice volume),^[25] similar to parameters used in the Materials Project.^[26] For calculations of the Eu^{2+} -doped $\text{K}_3\text{AlP}_3\text{O}_9\text{N}$ phosphors, a Hubbard U value of 2.5 eV was used to account for the highly correlated 4f electrons.^[27] Supercell models of $2 \times 2 \times 1$ (272 atoms) were constructed to approximate the low Eu^{2+} concentration in an experimental setting. All energies and forces were converged to within $1 \times 10^{-5} \text{ eV}$ and 0.01 eV \AA^{-1} , respectively.

The defect formation energies of Eu^{2+} substitution into $\text{K}_3\text{AlP}_3\text{O}_9\text{N}$ were calculated using the following equation,

$$\Delta E_f^d = E_{\text{tot}}^d - E_{\text{tot}}^b - \sum_i n_i \mu_i \quad (1)$$

where, E_{tot}^d and E_{tot}^b are the DFT calculated total energies of the Eu^{2+} substituted phosphor and $\text{K}_3\text{AlP}_3\text{O}_9\text{N}$ host, respectively, μ_i is the chemical potential of species i , and n_i indicates the number of atoms of species i being added ($n_i > 0$) or removed ($n_i < 0$).^[28] All crystal structure manipulations and data analysis were carried out using the Python Materials Genomics (Pymatgen) package.^[29]

3. Results and Discussion

3.1. Phase Pure Synthesis of an Efficient, Narrow Emitting, Oxynitride Phosphor

$\text{K}_3\text{AlP}_3\text{O}_9\text{N}$ can be synthesized through a gas-solid or solid-solid reaction between 600°C and 800°C where the nitrogen source can be ammonia, PON, a binary metal nitride, or $(\text{PNCl}_2)_3$.^[16] The majority of these methods involve air-sensitive precursors which require gloveboxes or Schlenk lines. Here, gas-reduction nitridation of oxide precursors under flowing NH_3 was used to synthesize $\text{K}_3\text{AlP}_3\text{O}_9\text{N}$ and the Eu^{2+} substituted phosphor. Interestingly, a single reaction at 800°C resulted in a mixture of an amorphous phase, likely a PON glass, and crystalline phases which could be indexed to $\text{K}_3\text{AlP}_3\text{O}_9\text{N}$ and $\text{K}_3\text{P}_6\text{N}_{11}$ (Figure S1a, Supporting Information). Repeating the sintering step removed the amorphous phase and resulted in a highly crystalline $\text{K}_3\text{AlP}_3\text{O}_9\text{N}$ product with a minor impurity of $\text{K}_3\text{P}_6\text{N}_{11}$, as seen

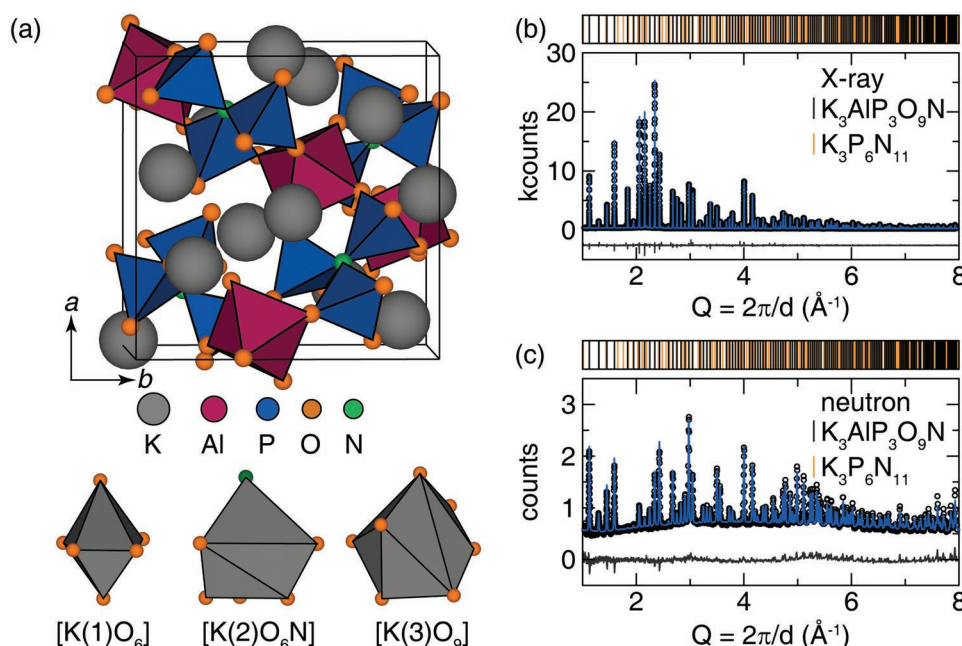


Figure 2. a) The crystal structure of $K_3AlP_3O_9N$ was solved through a corefinement of b) synchrotron powder X-ray diffraction and c) neutron scattering data. The crystal structure is composed of a backbone of $Al[N(PO_3)_3]_3$ clusters and three crystallographically independent K^+ atoms fill the voids.

in Figure S1b, present in the samples. Additional sintering steps had no effect on the purity of the sample.

$K_3AlP_3O_9N$ crystallizes in the cubic space group $P2_13$ (No. 198). As shown in Figure 2a, the crystal's unique backbone of $Al[N(PO_3)_3]_3$ clusters is composed of $[N(PO_3)_3]$ units that are made from three-fold coordinated $[PO_3]^-$ tetrahedra that share corners with $[AlO_6]$ octahedra. Three non-equivalent K^+ atoms are all located at different Wyckoff ($4a$) positions. $K(1)$ is octahedrally coordinated by oxygen, $K(2)$ is coordinated by six oxygen atoms and one nitrogen atom, and $K(3)$ is coordinated by nine oxygen atoms. The crystal structure of $K_3AlP_3O_9N$ was solved in 1994 using single-crystal X-ray diffraction (XRD).^[16] However, it is well-known that XRD is not able to unequivocally distinguish between oxygen and nitrogen due to their similar X-ray scattering factors. Fortunately, the neutron scattering cross sections of O (4.232 barns) and N (11.01 barns) are sufficiently different to determine any possible anion disorder.^[30] Therefore, the neutron data was first used to determine the identities of the anionic positions. The distribution of oxygen and nitrogen among the four anion sites within this crystal structure was approached similarly to the “coloring problem.”^[31] Starting from the original single crystal X-ray structure solution, the anion positions were arbitrarily assigned as an O or N.^[16] The neutron diffractogram was then refined using the Rietveld method and the most favorable anionic arrangement was selected based on the lowest refined R_p value. Next, disordered anionic positions were considered by manually mixing oxygen and nitrogen on each crystallographic position. The occupancies were again refined with the solution having the best R_p considered to be the preferred anion ordering. All of the refinement statistics are listed in Table S1, Supporting Information. From this analysis, the most suitable solution was achieved with oxygen fully occupying the three Wyckoff $12b$ positions and nitrogen occupying

the Wyckoff $4a$ position. Modeling four permutations of the O/N distribution in the anionic network with DFT yielded a similar site preference. The structure with nitrogen on Wyckoff $4a$ is the most energetically favorable by 360 meV per atom – 431 meV per atom (Table S1, Supporting Information). This places N at the center of three vertex-sharing phosphorous-centered tetrahedra, which is consistent with other phosphorous and silicon oxynitrides that contain bridging N^{3-} anions between corner-connected phosphorous or silicon-centered tetrahedra.^[16,32]

Co-refinements using a combination of high-resolution powder X-ray diffraction and neutron diffraction were then used to solve the crystal structure. The original single crystal structure was again input as the starting point with the $12b$ Wyckoff positions fully occupied by O and the $4a$ Wyckoff site filled by N. As plotted in Figures 2b,c, an excellent co-refined structure solution was obtained. All of the refined atomic positions are in agreement with the single crystal data and the ADPs are reasonable. It is also worth noting, the minor impurity phase $K_3P_6N_{11}$ was also included in the refinement. The refined product was found to contain 98(3)% of $K_3AlP_3O_9N$ and only 2(6)% of $K_3P_6N_{11}$, supporting the high purity of the oxynitride product. The resulting refined crystal structure data and atomic positions are listed in Table S2 and S3, Supporting Information.

The three crystallographically independent K^+ positions ($r_{6\text{-coord}} = 1.38 \text{ \AA}$; $r_{7\text{-coord}} = 1.46 \text{ \AA}$; $r_{9\text{-coord}} = 1.55 \text{ \AA}$) serve as the rare-earth substitution site because they are the only cationic sites large enough to accommodate Eu^{2+} ($r_{6\text{-coord}} = 1.17 \text{ \AA}$; $r_{7\text{-coord}} = 1.20 \text{ \AA}$; $r_{9\text{-coord}} = 1.30 \text{ \AA}$) unlike the P^{5+} ($r_{4\text{-coord}} = 0.17 \text{ \AA}$) or Al^{3+} ($r_{6\text{-coord}} = 0.535 \text{ \AA}$) sites.^[33] Substituting Eu^{2+} for K^+ following the nominal composition $K_{2.94}Eu_{0.03}AlP_3O_9N$ yields a bright blue emission ($\lambda_{em} = 454 \text{ nm}$) upon excitation from

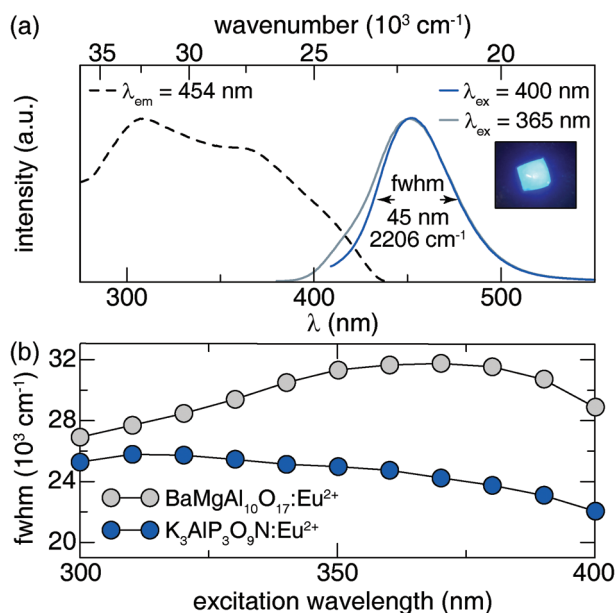


Figure 3. a) Excitation (black dashed line; $\lambda_{em} = 454 \text{ nm}$) spectrum of $K_{2.94}Eu_{0.03}AlP_3O_9N$. The emission band is centered at 454 nm with a different fwhm if UV (solid grey line) or violet (solid blue line) light excitation is used. $K_{2.94}Eu_{0.03}AlP_3O_9N$ has a narrow fwhm of only 45 nm (2206 cm^{-1}) upon violet light excitation. The inset shows the blue emission produced by $K_{2.94}Eu_{0.03}AlP_3O_9N$. b) The room temperature fwhm of $K_{2.94}Eu_{0.03}AlP_3O_9N$ (blue) is narrower than $BaMgAl_{10}O_{17}:Eu^{2+}$ (grey) across a range of excitation wavelengths spanning the UV and violet region.

260 nm–430 nm. This extremely wide excitation band contains three maxima centered at $\approx 310 \text{ nm}$, 365 nm, and 400 nm (Figure 3a). A prominent excitation band centered at 400 nm and the resulting small Stokes' shift is quite rare for blue-emitting phosphors since the majority of blue-emitting phosphors can only be excited by UV light.^[34] This red-shifted excitation band is likely due to the presence of N^{3-} within the host crystal structure, which induces a stronger nephelauxetic effect, along with the octahedral rare-earth substitution site that increases the rare-earth crystal field splitting.^[35] The result is a material with strong violet light absorption and small Stokes' shift enabling application as a blue-emitter in a human-centric lighting.

$K_{2.94}Eu_{0.03}AlP_3O_9N$ generates a bright blue photon emission upon UV or visible light excitation. Exciting the oxynitride with 365 nm light allows for the entirety of the emission spectrum to be captured (solid grey line, Figure 3a). This emission spectrum has a fwhm of 2457 cm^{-1} (50 nm) and contains two distinct features, including a high energy shoulder located between 400 nm and 450 nm and a dominating emission band centered at 454 nm. These emission peaks should stem from Eu^{2+} substituting on multiple K^+ sites. Shifting the excitation wavelength toward 420 nm light showed an exciting progression (Figure S2, Supporting Information). Using violet excitation ($\lambda_{ex} = 400 \text{ nm}$) revealed that the emission band, shown as the solid blue line in Figure 3a, is still centered at 454 nm, but the fwhm narrows significantly to 2206 cm^{-1} (45 nm). The evolution of the emission peak's fwhm is plotted in Figure 3b. The fwhm of $K_{2.94}Eu_{0.03}AlP_3O_9N$ upon 300 nm excitation is 2528 cm^{-1} (51 nm) while increasing the excitation wavelength to 400 nm

in 10 nm increments shows that the fwhm steadily decreases until a minimum is reached at 400 nm excitation. Interestingly, the excitation-dependent fwhm of commercially purchased $BaMgAl_{10}O_{17}:Eu^{2+}$ (grey), the current most viable blue-emitting phosphor for human-centric display backlighting, showed a very different trend. The fwhm of $BaMgAl_{10}O_{17}:Eu^{2+}$ is 2691 cm^{-1} (55 nm) upon 300 nm excitation and increasing the excitation wavelength causes the emission spectrum to steadily broaden until a maximum is reached at 370 nm excitation (3175 cm^{-1} , 65 nm). Beyond 370 nm excitation, the fwhm begins to incrementally decrease to 2888 cm^{-1} (59 nm) although it is still broader than $K_{2.94}Eu_{0.03}AlP_3O_9N$ with violet light excitation. It is clear that $K_{2.94}Eu_{0.03}AlP_3O_9N$ is a competitive phosphor for application considering it possesses a narrower emission band than commercial $BaMgAl_{10}O_{17}:Eu^{2+}$ regardless of excitation wavelength.

The origin of this optical response is revealed by analyzing the normalized emission spectra of each phosphor, plotted in Figure S3, Supporting Information. Increasing the excitation wavelength causes the emission spectra of $K_{2.94}Eu_{0.03}AlP_3O_9N$ to undergo a dramatic change in peak shape. Using a longer wavelength excitation preferentially excites the dominant emission band centered at 454 nm over the higher energy shoulder. The result is a continually narrowing emission band. $BaMgAl_{10}O_{17}:Eu^{2+}$, on the other hand, contains only one crystallographic site suitable for Eu^{2+} substitution, so preferential excitation cannot occur. As a result, the shape of the excitation wavelength-dependent emission spectra of $BaMgAl_{10}O_{17}:Eu^{2+}$ do not change. The expansion of the emission peak is likely due to subtle differences in electron-phonon coupling as a function of excitation wavelength.^[36] Thus, site-selective excitation in $K_{2.94}Eu_{0.03}AlP_3O_9N$ yields a very narrow blue-emission and small Stokes' shift that is ideal for human-centric display lighting.

Even though the initial analysis of this material's optical properties appears advantageous, to be applicable in human-centric displays $K_{2.94}Eu_{0.03}AlP_3O_9N$ must efficiently down-convert violet light to blue light. The room temperature internal photoluminescent quantum yield (PLQY) and external quantum yield (EQE) was measured using 400 nm excitation. $K_{2.94}Eu_{0.03}AlP_3O_9N$ has an optimized PLQY and EQE of 60(4)% and 22(1)%, respectively (Figure S4, Supporting Information). Further increasing the rare-earth concentration causes the PLQY to decrease to 40% due to concentration quenching. The optimized PLQY is higher than blue-emitting $Sr_{0.97}Eu_{0.03}Si_6N_8$ (PLQY = 38%, $\lambda_{ex} = 405 \text{ nm}$), but lower than industry standard $BaMgAl_{10}O_{17}:Eu^{2+}$ (PLQY = 90(1)%; $\lambda_{ex} = 400 \text{ nm}$).^[11,37] However, it is important to note that this commercially purchased $BaMgAl_{10}O_{17}:Eu^{2+}$ has likely undergone significant post-processing techniques such as additional sintering, improved particle morphology, and surface etching, among others, to improve the efficiency of the material.^[14] For example, without any post-processing, the photoluminescent quantum yield of lab-made $BaMgAl_{10}O_{17}:Eu^{2+}$ upon 400 nm excitation is less than 25%.^[38] The PLQY and EQE of $K_{2.94}Eu_{0.03}AlP_3O_9N$ could undoubtedly be vastly improved through industrial post-processing techniques. Therefore, the combination of the reasonable PLQY out of the furnace and the narrow emission band upon 400 nm excitation is uncommon for the majority

of blue-emitting phosphors, making $K_{2.94}Eu_{0.03}AlP_3O_9N$ one of few materials that currently meet the minimum requirements for human-centric display lighting.

3.2. Narrowing the Emission Peak: Site Selective Excitation and Preferential Quenching

The narrow emission band from $K_{2.94}Eu_{0.03}AlP_3O_9N$ is crucial for utilizing this phosphor in LED-based displays. It is especially surprising that the emission is so narrow upon violet light excitation considering that there are three crystallographically independent rare-earth substitution sites, [K(1)O₆], [K(2)O₆N], and [K(3)O₉], within the host crystal structure that are

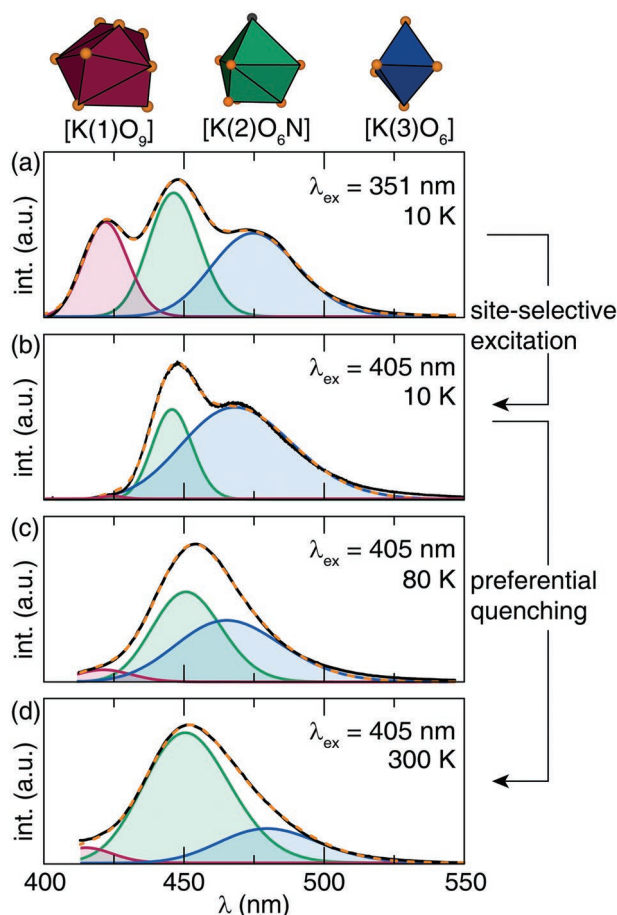


Figure 4. a) Lowering the temperature to 10 K and exciting $K_{2.94}Eu_{0.03}AlP_3O_9N$ with UV ($\lambda_{ex} = 351$ nm) light reveals three distinct emission bands stemming from Eu^{2+} substitution on the three crystallographically independent K^+ sites. Performing a Gaussian deconvolution allows the Van Uitert equation to be used to assign the emission bands at 422 nm (red), 446 nm (green), and 475 nm (blue) to Eu^{2+} on [K(1)O₆], [K(2)O₆N], and [K(3)O₉], respectively. b) Exciting $K_{2.94}Eu_{0.03}AlP_3O_9N$ at 10 K with violet ($\lambda_{ex} = 405$ nm) light shows the extent of the site-selective excitation where the emission from Eu^{2+} on [K(2)O₆N] and [K(3)O₉] dominate over the emission from [K(1)O₆]. Increasing the temperature to c) 80 K and d) 300 K but keeping violet ($\lambda_{ex} = 405$ nm) excitation shows that the emission from [K(3)O₉] preferentially quenches. The combination of these effects causes the observed narrow blue emission band from $K_{2.94}Eu_{0.03}AlP_3O_9N$.

large enough to accommodate Eu^{2+} . The site preference of Eu^{2+} in $K_3AlP_3O_9N$ was thus investigated using DFT calculations. To maintain overall charge neutrality, the aliovalent substitution of Eu^{2+} for K^+ must be compensated by the formation of other defects. Two charge-neutral defect configurations (ΔE_f^d), denoted in Kröger-Vink notation, were considered where \times , \cdot , and \prime refer to neutral, positively charged, and negatively charged point defects, respectively, and V refers to a vacancy site.^[39]



For each defect configuration, over 60 symmetrically distinct orderings were optimized and the differences in the total energies are plotted in Figure S5, Supporting Information. The dopant formation energy (E_f^d) of the lowest energy configuration containing N'_O (Equation 2) is 235 meV per defect, which is sufficiently high enough to rule out this defect compensation mechanism. This is also consistent with the results of the co-refinement where the O and N positions refined to be fully occupied. In contrast, the defect formation energies for the structures containing the V'_K (Equation 3) are generally less than 10 meV/defect and fall within a range of less than 6 meV per atom (Table S4, Supporting Information).^[40] Based on these calculations, Eu^{2+} substitution results in the formation of K^+ vacancies, and there is no energetic preference for Eu^{2+} to preferentially substitute on a particular K^+ site.

Taking into consideration that there is no strong energetic site preference for rare-earth substitution, the emission spectrum of $K_{2.94}Eu_{0.03}AlP_3O_9N$ should be composed of three distinct emission bands. However, the room temperature photoluminescence spectrum of $K_{2.94}Eu_{0.03}AlP_3O_9N$ when excited by UV or violet light does not display three distinct emission bands. Only one broad peak (with a small shoulder) is observed. Photoluminescent measurements were consequently conducted at 10 K to conclusively resolve the emission bands. Lowering the temperature to 10 K and exciting with UV light ($\lambda_{ex} = 351$ nm), as plotted in Figure 4a, reveals three well-defined emission bands arising from Eu^{2+} substitution on all three K^+ sites, as anticipated. Considering that no additional emission is observed, the slight impurity of $K_3P_6N_{11}$ ($\approx 2\%$) has no effect on the observed photoluminescence of $K_{2.94}Eu_{0.03}AlP_3O_9N$ even at low temperatures. A Gaussian deconvolution was performed to determine that the three peaks are centered at $\lambda_{em} = 422$ nm (red), 446 nm (green), and 475 nm (blue). The Van Uitert equation can then be used to assign the probable substitution site generating each emission peak.

$$E \text{ (cm}^{-1}\text{)} = Q \left[1 - \left(\frac{V}{4} \right)^{\frac{1}{V}} 10^{-n E_a r / 80} \right] \quad (4)$$

As provided in Equation 4, E is the energy of the emission, Q is the position of the lower d-band edge of a free Eu^{2+} ion or $34\,000 \text{ cm}^{-1}$, V is the valency of the activator, n is the number of coordinating anions around the activator, E_a is the electron affinity of the coordinating anions, and r is the radius of the host cation replaced by the activator.^[41] Using the refined polyhedral

coordination environments, Eu^{2+} in the $[\text{K}(1)\text{O}_9]$, $[\text{K}(2)\text{O}_6\text{N}]$, and $[\text{K}(3)\text{O}_6]$ positions are calculated to emit at $\approx 25\,188\text{ cm}^{-1}$ (397 nm), $21\,226\text{ cm}^{-1}$ (471 nm), and $20\,750\text{ cm}^{-1}$ (482 nm), respectively. This is in excellent agreement with the experimentally measured photoluminescence data with the emission peak centered at 422 nm produced by Eu^{2+} substituted on $[\text{K}(1)\text{O}_9]$, the peak at 446 nm stemming from Eu^{2+} on $[\text{K}(2)\text{O}_6\text{N}]$, and the peak at 475 nm arising from Eu^{2+} on $[\text{K}(3)\text{O}_6]$.

Exciting $\text{K}_{2.94}\text{Eu}_{0.03}\text{AlP}_3\text{O}_9\text{N}$ with violet light ($\lambda_{\text{ex}} = 405\text{ nm}$) at 10 K, shown in Figure 4b, clearly depicts the magnitude of the preferential excitation. The emission from Eu^{2+} on the $[\text{K}(2)\text{O}_6\text{N}]$ and $[\text{K}(3)\text{O}_6]$ sites dominate over the emission from the $[\text{K}(1)\text{O}_9]$. Violet light is insufficient to excite this high-energy band. As a result of this site-selective excitation, the total emission spectrum narrows significantly from 70 nm (3480 cm^{-1}) to only 45 nm (2140 cm^{-1}).

$\text{K}_{2.94}\text{Eu}_{0.03}\text{AlP}_3\text{O}_9\text{N}$ has another intrinsic advantage that enables such a narrow emission. Increasing the temperature to 80 K (Figure 4c) and then 300 K (Figure 4d) shows the peak centered at 475 nm stemming from Eu^{2+} on the $[\text{K}(3)\text{O}_6]$ site undergoes significant preferential thermal quenching. This anomalous response explains the origin of the narrow blue emission from $\text{K}_{2.94}\text{Eu}_{0.03}\text{AlP}_3\text{O}_9\text{N}$. The preferential quenching behavior can be explained by calculating the Stokes' shift of each emission peak and relating it to electron-phonon coupling, which is one way to describe the probability of nonradiative relaxation through the crossover mechanism. The electron-phonon coupling strength can be approximated by the Huang–Rhys parameter, S , through the Stokes' shift (E_{Stokes}), as shown in Equation 5.

$$S = \left(\frac{1}{2} \frac{E_{\text{Stokes}}}{\hbar\omega} + \frac{1}{4} \right) \pm \frac{1}{4} \quad (5)$$

The vibrational energy, $\hbar\omega$, can only be determined when the vibrational fine structure is available. However, as seen in Figure 4, this data is not resolved even at 10 K making it impossible to quantitatively determine S . Still, a qualitative analysis can still be carried out based on E_{Stokes} . In $\text{K}_{2.94}\text{Eu}_{0.03}\text{AlP}_3\text{O}_9\text{N}$, the emission peak centered at 446 nm has a Stokes' shift of 2595 cm^{-1} whereas the emission peak centered at 475 nm has a far larger Stokes' shift of 3931 cm^{-1} . As a result, the low energy emission band should have a larger value of S and should exhibit more electron-phonon coupling. This increases the likelihood of the occurrence of a cross-over between the ground state and excited state potential energy surfaces, which acts as a nonradiative pathway. Ultimately, the combination of these two phenomena, site-selective excitation, and preferential quenching, gives rise to the highly desirable efficient and narrow emission in $\text{K}_{2.94}\text{Eu}_{0.03}\text{AlP}_3\text{O}_9\text{N}$.

Finally, the thermal quenching response of $\text{K}_{2.94}\text{Eu}_{0.03}\text{AlP}_3\text{O}_9\text{N}$ from 300 K to 640 K was examined to determine the phosphor's applicability in LED-driven display lighting. The temperature-dependent emission spectra are plotted in Figure S6a, Supporting Information. The spectra reveal an anomalous increase in the emission intensity as a function of temperature, presumably caused by the release of trapped photons from defect states. These defect states are the K^+ vacancies that are generated to maintain charge balance after

the aliovalent substitution of Eu^{2+} . This further corroborates the charge compensation mechanism determined by DFT. Normalizing the temperature-dependent emission spectra, shown in Figure S6b, Supporting Information, indicates that the emission spectrum slightly blueshifts and broadens as a function of temperature. Both of these phenomena are common for rare-earth substituted phosphors. The subtle temperature-induced blueshift from $\lambda_{\text{em,max}} = 454\text{ nm}$ to $\lambda_{\text{em,max}} = 450\text{ nm}$ most likely results from the thermal expansion of the unit cell.^[42] The increase in the fwhm from 2066 cm^{-1} (300 K) to 2944 cm^{-1} (640 K) can be attributed to an increase in the electron-phonon coupling at elevated temperatures.^[36] The combination of photon de-trapping and an increase in the fwhm results in zero thermal quenching of the emission up to 640 K (Figure S6c, Supporting Information) making $\text{K}_{2.94}\text{Eu}_{0.03}\text{AlP}_3\text{O}_9\text{N}$ a promising candidate for LED-based display lighting.

3.3. Enabling a Wide-Gamut, Human-Centric Display Backlighting

Human-centric displays aim to replace blue LEDs with a blue-emitting phosphor in the screen's backlight unit. As a result, the phosphor must have similar or more saturated 1931 CIE XYZ color coordinates than the (InGa)N LED to warrant the switch. The potential of $\text{K}_{2.94}\text{Eu}_{0.03}\text{AlP}_3\text{O}_9\text{N}$ to be used in LED displays was first investigated by comparing the chromaticity coordinates of the oxynitride phosphor to a blue LED as well as commercial $\text{BaMgAl}_{10}\text{O}_{17}:\text{Eu}^{2+}$. The chromaticity coordinates of the three blue emitters were plotted on a 1931 CIE XYZ diagram, shown in Figure 5a. Commercial $\text{BaMgAl}_{10}\text{O}_{17}:\text{Eu}^{2+}$ (white square), unsurprisingly, has the least saturated color coordinates and lies furthest away from the vertex of the Rec. 2020 (white line) due to its wide emission band with violet (400 nm) excitation. In contrast, the blue LED (white triangle) and $\text{K}_{2.94}\text{Eu}_{0.03}\text{AlP}_3\text{O}_9\text{N}$ (white circle) produce a deeper blue color with $\text{K}_{2.94}\text{Eu}_{0.03}\text{AlP}_3\text{O}_9\text{N}$ being closer to the vertex of the Rec. 2020. This indicates that $\text{K}_{2.94}\text{Eu}_{0.03}\text{AlP}_3\text{O}_9\text{N}$ is not only a suitable blue emitter for human-centric displays, but using this phosphor can allow for access to a wider range of colors in modern LED-based displays.

The second aspect of transitioning to human-centric displays is to consider the presence of a violet LED instead of a blue LED. A model white backlight spectrum can be produced by combining a violet LED ($\lambda_{\text{em}} \approx 395\text{ nm}$) with a mixture of $\text{K}_{2.94}\text{Eu}_{0.03}\text{AlP}_3\text{O}_9\text{N}$, $\beta\text{-SiAlON}:\text{Eu}^{2+}$, and $\text{CaAlSiN}_3:\text{Eu}^{2+}$. The green and red phosphors were chosen due to their excellent absorption of violet light (Figure S7, Supporting Information) and application in real display units. This white backlight spectrum, plotted in Figure 5b, was tuned to produce 1931 CIE coordinates at (0.3146, 0.3218) with a correlated color temperature of 6452 K, which closely matches the white point of a D65 standard illuminant used to analyze modern televisions.^[43] The general color rendering index, R_a , of the model white backlight is 78. Since the color rendering index is used to evaluate the color rendering capabilities of general illumination light bulbs, the backlight is penalized due to the gaps in the white light spectrum arising from the narrow fwhm of the LED and phosphor emission.^[44] Instead, the color rendering capabilities

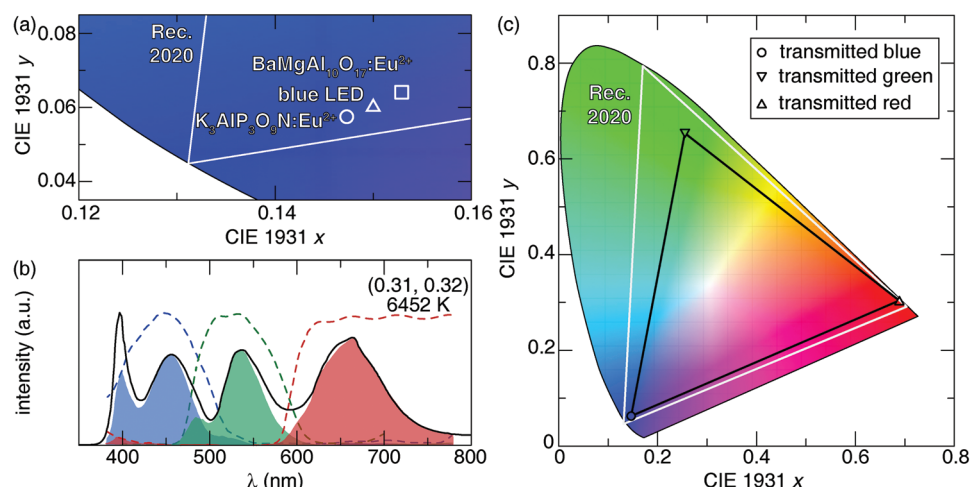


Figure 5. a) The 1931 CIE XYZ chromaticity coordinates of commercially purchased $\text{BaMgAl}_{10}\text{O}_{17}:\text{Eu}^{2+}$ (square), a blue LED (triangle), and $\text{K}_{2.94}\text{Eu}_{0.03}\text{AlP}_3\text{O}_9\text{N}$ (circle). The blue LED coordinates were taken from ref. [38]. $\text{K}_{2.94}\text{Eu}_{0.03}\text{AlP}_3\text{O}_9\text{N}$ has 1931 CIE XYZ coordinates of (0.147, 0.058). b) A model white light spectrum produced by combining a violet LED ($\lambda_{\text{em}} \approx 395$ nm) with a mixture of $\text{K}_{2.94}\text{Eu}_{0.03}\text{AlP}_3\text{O}_9\text{N}$, $\beta\text{-SiAlON}:\text{Eu}^{2+}$, and $\text{CaAlSi}_3\text{N}_3:\text{Eu}^{2+}$ has 1931 CIE coordinates of (0.31, 0.32) with a correlated color temperature of 6452 K, corresponding to the D65 standard illuminant. The transmittance spectra of red, green, and blue liquid crystal display (LCD) color filters are shown as the dashed red, green, and blue lines. The portions of the white light spectrum that are allowed to pass through each filter are represented by the shaded regions. c) The CIE coordinates of the blue, green, and red emission that can pass through the filters is represented by the circle, down triangle, and up triangle, respectively.

of display backlights are more accurately quantified using the television lighting consistency index (TLCI-2012). The TLCI-2012 evaluates the color rendering of a test light source against 24 standard color samples and yields a score out of 100, where 100 indicates perfect color rendering.^[45] The TLCI-2012 score of the model backlight when compared against a standard D65 standard illuminant is 53 and is similar to the Apple iPad® which has a score of 60, indicating that our violet-LED driven device has comparable color rendering capabilities to a commercial display. Finally, the luminance efficacy of radiation (LER), which is a measure of the power conversion capabilities of the model spectrum is 188 lm W^{-1} . The LER of the commercial iPad is 341 lm W^{-1} . While there is a notable difference between the LER of both devices, it is important to note that using a 405 nm LED instead of a 450 nm LED automatically leads to $\approx 10\%$ loss in the LER due to the Stokes loss from the down-conversion process. Moreover, improving the wall-plug efficiency of violet LEDs will lessen this penalty and improve the overall LER of human-centric displays, making them competitive with traditional blue LED driven-devices.

The basic gamut coverage provides only part of the optical property information from a backlight display. The white light passes through a red, green, and blue color filter (dashed lines, Figure 5b), which not only creates the color images but also sets the display's color gamut and energy efficiency. Thus, it is imperative that the violet LED and blue phosphor emission are compatible with these filters. The portions of the white light spectrum that can be transmitted through each filter are depicted in Figure 5b as the shaded red, green, and blue regions. The entire emission spectrum of $\text{K}_{2.94}\text{Eu}_{0.03}\text{AlP}_3\text{O}_9\text{N}$ is able to pass through the blue color filter due to the position of the emission band ($\lambda_{\text{em}} = 454$ nm) and its narrow fwhm. The narrow emission band also helps to minimize overlap (crosstalk) with the green color filter, but it is clear that additional

improvement to the fwhm of the blue and more so the green emission peaks must occur to further limit crosstalk. The chosen green- and red-emitting phosphors also match well with the transmission spectra of the color filters, indicating that a display utilizing this trichromatic phosphor mixture may have a high transfer efficiency and total light efficiency.^[46] The violet LED emission also passes through the blue color filter, but the signal is slightly attenuated due to the lower transmittance at shorter wavelengths. The chromaticity coordinates of the resulting display gamut were obtained from the filtered emission spectra and plotted in Figure 5c. This gamut covers 68% of the Rec. 2020, which is 9% more than an Apple iPad (Figure S8, Supporting Information), which only covers 62%. The less-than-complete coverage of the Rec. 2020 is largely due to the chromaticity coordinates of commercial $\beta\text{-SiAlON}:\text{Eu}^{2+}$, which is not as saturated as necessary to meet Rec. 2020 requirements. This issue is present in every display that uses this green phosphor. Regardless, the combination of the violet LED emission and bright blue emission from $\text{K}_{2.94}\text{Eu}_{0.03}\text{AlP}_3\text{O}_9\text{N}$ still yields incredibly saturated chromaticity coordinates that lie within the Rec. 2020 and near the vertex of the deep blue region. Thus, this violet LED-based backlight is capable of producing a wide color gamut that satisfies over two-thirds of the Rec. 2020 (more than a commercial tablet), and the entirety of the deep blue region.

Finally, the potential of $\text{K}_{2.94}\text{Eu}_{0.03}\text{AlP}_3\text{O}_9\text{N}$ for human-centric-based displays is reinforced by plotting the wavelength-dependent melatonin suppression curve on the model white backlight, shown in Figure 6. This white backlight was constructed to not only mimic the white point of a D65 standard illuminant, but also to intentionally minimize the amount of blue light emitted. Since the LED emission, which is the most intense emission in the device, falls mostly outside the maximum of the wavelength-dependent melatonin suppression

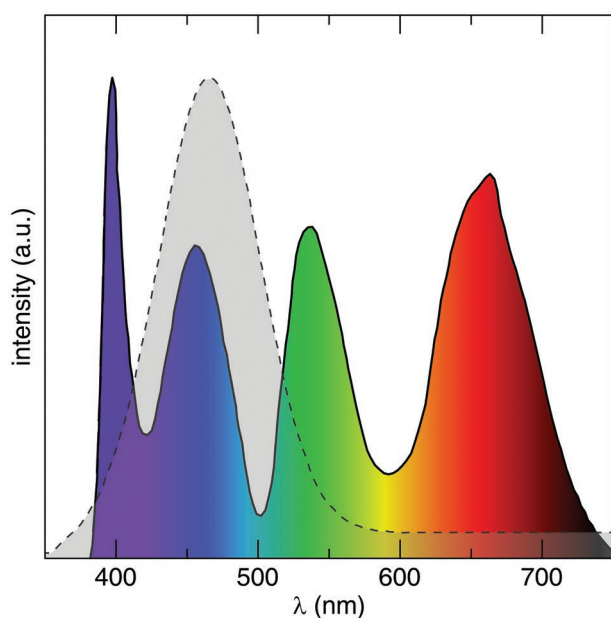


Figure 6. Applying a wavelength-dependent melatonin suppression curve (dashed, grey) over the white backlight shows the blue phosphor emission is minimized and the intense LED signal has little effect on melatonin suppression.

curve, melatonin production should not be significantly disturbed even if the LED is driven on high brightness mode using this device design. These results convey the capability of $K_{2.94}Eu_{0.03}AlP_3O_9N$ for producing a wide gamut, a human-centric display screen that minimizes melatonin suppression and may also begin addressing the many other ailments connected with the continual exposure to this blue-light hazard.

4. Conclusion

Eu^{2+} -substituted $K_3AlP_3O_9N$ was synthesized using gas reduction nitridation. The anionic positions within the crystal structure were confirmed through joint synchrotron X-ray and neutron powder diffraction. Optical characterization revealed that $K_{2.94}Eu_{0.03}AlP_3O_9N$ could be excited by violet LED light to produce an efficient (PLQY = 60(4)%) and narrow blue emission (fwhm = 45 nm; 2206 cm^{-1}). These optical properties were surprising considering the host crystal structure contains three crystallographically independent K^+ sites for rare-earth substitution. DFT calculations confirmed no energetic driving force for preferential substitution and support that the narrow emission stems a combination of preferential excitation and site-selective quenching. Ultimately, the narrow blue emission band of $K_3AlP_3O_9N:Eu^{2+}$ yields 1931 CIE XYZ coordinates that are more saturated than the blue color coordinates of commercial $BaMgAl_{10}O_{17}:Eu^{2+}$ and a blue LED chip. Further, utilizing a violet LED and $K_{2.94}Eu_{0.03}AlP_3O_9N$ in a human-centric display creates a wide gamut that covers 9% more of the Rec. 2020 than a commercial tablet while careful tuning of the violet LED and trichromatic phosphor mixture emission can reduce the amount of blue light emitted. The exceptional optical properties of $K_{2.94}Eu_{0.03}AlP_3O_9N$ undoubtedly pave the way for a new

direction in display technologies with the end user's health in mind.

Supporting Information

Supporting Information is available from the Wiley Online Library or from the author.

Acknowledgements

S.H. would like to thank Jacob Hickey for his advice and support in building the furnace utilized in this work. S.H. and J.B. like to thank the National Science Foundation (CER-1911311) as well as the Welch Foundation (E-1981) for supporting this work. J.M.B. acknowledged support from Welch Foundation (E-1728). M.A. and S.P.O. acknowledged funding from the National Science Foundation (CER-1911372), computing resources provided by the National Energy Research Scientific Computing Center (NERSC) under Contract No. DE-AC02-05CH11231 using NERSC award BESERCAP0018251, the Triton Shared Computing Cluster (TSCC) at the University of California, San Diego, and the Extreme Science and Engineering Discovery Environment (XSEDE) under grant ACI-1548562. This work used the resources available through the 11-BM beamline at the Advanced Photon Source, an Office of Science User Facility operated for the U.S. Department of Energy (DOE) Office of Science by Argonne National Laboratory, under Contract No. DE-AC02-06CH11357.

Conflict of Interest

The authors declare no conflict of interest.

Data Availability Statement

The data that support the findings of this study are available from the corresponding author upon reasonable request.

Keywords

ab initio calculations, human-centric lighting, melatonin suppression, phosphorous oxynitride, violet-excitation

Received: November 18, 2022

Revised: January 5, 2023

Published online:

- [1] a) S. Nakamura, *Science* **1998**, 281, 956; b) P. Pust, P. J. Schmidt, W. Schnick, *Nat. Mater.* **2015**, 14, 454; c) Y. Nanishi, *Nat. Photonics* **2014**, 8, 884.
- [2] H.-W. Chen, R.-D. Zhu, J. He, W. Duan, W. Hu, Y.-Q. Lu, M.-C. Li, S.-L. Lee, Y.-J. Dong, S.-T. Wu, *Light Sci Appl* **2017**, 6, e17043.
- [3] H.-J. Kim, M.-H. Shin, J.-Y. Lee, J.-H. Kim, Y.-J. Kim, *Opt. Express* **2017**, 25, 10724.
- [4] a) P. Pust, V. Weiler, C. Hecht, A. Tücks, A. S. Wochnik, A.-K. Henß, D. Wiechert, C. Scheu, P. J. Schmidt, W. Schnick, *Nat. Mater.* **2014**, 13, 891; b) J. E. Murphy, F. Garcia-Santamaria, A. A. Setlur, S. Sista, *SID Int. Symp. Dig. Tech. Pap.* **2015**, 46, 927; c) Y. Li, X. Hou, X. Dai, Z. Yao, L. Lv, Y. Jin, X. Peng, *J. Am. Chem. Soc.* **2019**, 141, 6448.

- [5] a) M. Zhao, H. Liao, L. Ning, Q. Zhang, Q. Liu, Z. Xia, *Adv. Mater.* **2018**, 30, 1802489; b) Z. Wu, C. Li, F. Zhang, S. Huang, F. Wang, X. Wang, H. Jiao, *J. Mater. Chem. C* **2022**, 10, 7443.
- [6] L. S. Mure, F. Vinberg, A. Hanneken, S. Panda, *Science* **2019**, 366, 1251.
- [7] a) J. Hye Oh, S. Ji Yang, Y. Rag Do, *Light Sci Appl* **2014**, 3, e141; b) W. Tang, J. G. Liu, C. Shen, *IEEE Photonics J.* **2018**, 10, 8201210.
- [8] R. Nagare, B. Plitnick, M. Figueiro, *Light. Rec. Technol.* **2019**, 51, 373.
- [9] M. Gradisar, A. R. Wolfson, A. G. Harvey, L. Hale, R. Rosenberg, C. A. Czeisler, *J. Clin. Sleep Med.* **2013**, 09, 1291.
- [10] H. Daicho, T. Iwasaki, K. Enomoto, Y. Sasaki, Y. Maeno, Y. Shinomiya, S. Aoyagi, E. Nishibori, M. Sakata, H. Sawa, S. Matsuishi, H. Hosono, *Nat. Commun.* **2012**, 3, 1132.
- [11] S. Hariyani, J. Brgoch, *ACS Appl. Mater. Interfaces* **2021**, 13, 16669.
- [12] A. D. Fobian, K. Avis, D. C. Schwebel, *J. Dev. Behav. Pediatr* **2016**, 37, 9.
- [13] J. Qiao, L. Ning, M. S. Molokeev, Y.-C. Chuang, Q. Liu, Z. Xia, *J. Am. Chem. Soc.* **2018**, 140, 9730.
- [14] L.-J. Yin, J. Dong, Y. Wang, B. Zhang, Z.-Y. Zhou, X. Jian, M. Wu, X. Xu, J. R. van Ommen, H. T. Hintzen, *J. Phys. Chem. C* **2016**, 120, 2355.
- [15] S. Wendl, L. Eisenburger, P. Strobel, D. Günther, J. P. Wright, P. J. Schmidt, O. Oeckler, W. Schnick, *Chem. - Eur. J.* **2020**, 26, 7292.
- [16] R. Marchand, W. Schnick, N. Stock, *Adv. Inorg. Chem.* **2000**, 50, 193.
- [17] R. Conanec, W. Feldmann, R. Marchand, Y. Laurent, *J. Solid State Chem.* **1996**, 121, 418.
- [18] J.-H. Park, K.-S. Lee, B.-C. Choi, *J. Phys.: Condens. Matter* **2001**, 13, 9411.
- [19] J. Wang, B. H. Toby, P. L. Lee, L. Ribaud, S. M. Antao, C. Kurtz, M. Ramanathan, R. B. V. Dreele, M. A. Beno, *Rev. Sci. Instrum.* **2008**, 79, 085105.
- [20] K. A. Denault, J. Brgoch, S. D. Kloss, M. W. Gaultois, J. Siewenie, K. Page, R. Seshadri, *ACS Appl. Mater. Interfaces* **2015**, 7, 7264.
- [21] a) B. H. Toby, *J. Appl. Crystallogr.* **2001**, 34, 210; b) A. C. Larson, R. B. Von Dreele, *Generalized Structure Analysis System (GSAS)*, Report LAUR 86-748, Los Alamos National Laboratory, Los Alamos, NM **1994**.
- [22] K. Momma, F. Izumi, *J. Appl. Crystallogr.* **2011**, 44, 1272.
- [23] S. Leyre, E. Coutino-Gonzalez, J. J. Joos, J. Ryckaert, Y. Meuret, D. Poelman, P. F. Smet, G. Durinck, J. Hofkens, G. Deconinck, P. Hanselaer, *Rev. Sci. Instrum.* **2014**, 85, 123115.
- [24] a) G. Kresse, J. Furthmüller, *Phys. Rev. B: Condens. Matter Mater. Phys.* **1996**, 54, 11169; b) P. E. Blöchl, *Phys. Rev. B: Condens. Matter Mater. Phys.* **1994**, 50, 17953.
- [25] W. Sun, S. T. Dacek, S. P. Ong, G. Hautier, A. Jain, W. D. Richards, A. C. Gamst, K. A. Persson, G. Ceder, *Sci. Adv.* **2016**, 2, e1600225.
- [26] A. Jain, S. P. Ong, G. Hautier, W. Chen, W. D. Richards, S. Dacek, S. Cholia, D. Gunter, D. Skinner, G. Ceder, K. A. Persson, *APL Mater.* **2013**, 1, 011002.
- [27] a) S. L. Dudarev, G. A. Botton, S. Y. Savrasov, C. J. Humphreys, A. P. Sutton, *Phys. Rev. B: Condens. Matter Mater. Phys.* **1998**, 57, 1505; b) A. Chaudhry, R. Boutchko, S. Chourou, G. Zhang, N. Grønbech-Jensen, A. Canning, *Phys. Rev. B: Condens. Matter Mater. Phys.* **2014**, 89, 155105.
- [28] S.-H. Wei, S. B. Zhang, *Phys. Rev. B: Condens. Matter Mater. Phys.* **2002**, 66, 155211.
- [29] S. P. Ong, W. D. Richards, A. Jain, G. Hautier, M. Kocher, S. Cholia, D. Gunter, V. L. Chevrier, K. A. Persson, G. Ceder, *Comput. Mater. Sci.* **2013**, 68, 314.
- [30] a) P. Bacher, P. Antoine, R. Marchand, P. L'Haridon, Y. Laurent, G. Rault, *J. Solid State Chem.* **1988**, 77, 67; b) V. F. Sears, *J. Neutron Res.* **1992**, 3, 26.
- [31] G. J. Miller, *Eur. J. Inorg. Chem.* **1998**, 1998, 523.
- [32] R.-J. Xie, N. Hirotsaki, *Sci. Technol. Adv. Mater.* **2007**, 8, 588.
- [33] R. D. Shannon, *Acta Crystallogr* **1976**, A32, 751.
- [34] V. B. Pawade, H. C. Swart, S. J. Dhoble, *Renew. Sustainable Energy Rev.* **2015**, 52, 596.
- [35] N. C. George, K. A. Denault, R. Seshadri, *Annu. Rev. Mater. Res.* **2013**, 43, 481.
- [36] Y. Zhuo, A. Mansouri Tehrani, A. O. Oliynyk, A. C. Duke, J. Brgoch, *Nat. Commun.* **2018**, 9, 4377.
- [37] K. Shioi, N. Hirotsaki, R.-J. Xie, T. Takeda, Y. Li, *J. Mater. Sci.* **2008**, 43, 5659.
- [38] A. C. Duke, S. Hariyani, J. Brgoch, *Chem. Mater.* **2018**, 30, 2668.
- [39] F. A. Kröger, H. J. Vink, in *Solid State Physics* (Eds: F. Seitz, D. Turnbull), Vol. 3, Academic Press, New York **1956**, pp. 307-435.
- [40] S. G. Jantz, R. Erdmann, S. Hariyani, J. Brgoch, H. A. Höppe, *Chem. Mater.* **2020**, 32, 8587.
- [41] L. G. van Uitert, *J. Lumin.* **1984**, 29, 1.
- [42] S. You, Y. Zhuo, Q. Chen, J. Brgoch, R.-J. Xie, *J. Mater. Chem. C* **2020**, 8, 15626.
- [43] K. Choi, T. Kim, J. Chang, H. Suk, *IEEE Trans. Broadcast Telev. Receivers* **2018**, 64, 292.
- [44] S. Hariyani, J. Brgoch, *Inorg. Chem.* **2022**, 61, 4205.
- [45] P. Böhrer, J. Emmett, A. Roberts, *SMPTE J.* **2013**, 122, 30.
- [46] Z. Luo, Y. Chen, S.-T. Wu, *Opt. Express* **2013**, 21, 26269.